International Journal of Applied Earth Observation and Geoinformation 23 (2013) 226–233

Contents lists available at SciVerse ScienceDirect

International Journal of Applied Earth Observation and Geoinformation

journal homepage: www.elsevier.com/locate/jag

Validation of the SEBS-derived sensible heat for FY3A/VIRR and TERRA/MODIS over an alpine grass region using LAS measurements

Yuanyuan Wang[a,*], Xiang Li[a,b], Shihao Tang[a]

[a] Key Laboratory of Radiometric Calibration and Validation for Environmental Satellites, China Meteorological Administration (LRCVES/CMA), and the National Satellite Meteorological Center, China Meteorological Administration, Beijing, PR China
[b] Applied Meteorology College, Nanjing University of Information Science & Technology, Nanjing, PR China

ARTICLE INFO

Article history:
Received 4 May 2012
Accepted 17 September 2012

Keywords:
SEBS
Sensible heat
VIRR
MODIS
LAS

ABSTRACT

In this study, sensible heat (H) calculation using remote sensing data over an alpine grass landscape is conducted from May to September 2010, and the calculation is validated using LAS (large aperture scintillometers) measurements. Data from two remote sensing sensors (FY3A-VIRR and TERRA-MODIS) are analysed. Remote sensing data, combined with the ground meteorological observations (pressure, temperature, wind speed, humidity) are fed into the SEBS (Surface Energy Balance System) model. Then the VIRR-derived sensible heat (VIRR_SEBS_H) and MODIS-derived sensible heat (MODIS_SEBS_H) are compared with the LAS-estimated *H*, which are obtained at the respective satellite overpass time. Furthermore, the similarities and differences between the VIRR_SEBS_H and MODIS_SEBS_H values are investigated. The results indicate that VIRR data quality is as good as MODIS data for the purpose of *H* estimation. The root mean square errors (*rmse*) of the VIRR_SEBS_H and MODIS_SEBS_H values are 45.1098 W/m^2 (n = 64) and 58.4654 W/m^2 (n = 71), respectively. The monthly means of the MODIS_SEBS_H are marginally higher than those of VIRR_SEBS_H because the satellite overpass time of the TERRA satellite lags by 25 min to that of the FT3A satellite. Relative evaporation (EFr), which is more time-independent, shows a higher agreement between MODIS and VIRR. Many common features are shared by the VIRR_SEBS_H and the MODIS_SEBS_H, which can be attributed to the SEBS model performance. In May–June, *H* is over-estimated with more fluctuations and larger *rmse*, whereas in July–September, *H* is under-estimated with fewer fluctuations and smaller *rmse*. Sensitivity analysis shows that potential temperature gradient (delta_*T*) plays a dominant role in determining the magnitude and fluctuation of *H*. The largest *rmse* and over-estimation in *H* occur in June, which could most likely be attributed to high delta_*T*, high wind speed, and the complicated thermodynamic state during the transitional period when bare land transforms to dense vegetation cover.

1. Introduction

Sensible heat (H) and latent heat (LE) flux are the key components in the energy and mass exchange budget among the atmosphere, hydrosphere, and biosphere (Su, 2002). Accurate quantification of *H* and LE, and their spatio-temporal pattern has been a topic of discussion in many disciplines (van der Kwast et al., 2009). Remote sensing is by far the only technique that is able to provide *H* and LE information at a regional scale with various spatio-temporal resolutions. Many methods have been developed in the past using remote sensing data to estimate *H* and LE, such as the SEBS (Surface Energy Balance System, Su, 2002), SEBI (Surface Energy Balance Index, Roerink et al., 2000), SEBAL (Surface Energy Balance Algorithms for Land, Bastiaanssen, 2000), TSEB (Two Source Energy Balance, Norman et al., 1995) model, METRIC (Mapping EvapoTranspiration at high Resolution with Internal Calibration, Allen et al., 2007) model, and TVT (Temperature and Vegetation Index Triangle, Moran et al., 1994). These models and methods vary greatly in the principles (process-based or not, single source or dual source), inputs, assumptions, and the degree of dependency on ground-based auxiliary measurements (Courault et al., 2005; Li et al., 2009). Comparison of the different models for *H* and LE estimation at the local or global scale has demonstrated a variable degree of success for the different models (Timmermans et al., 2005; Vinukollu et al., 2011; Tang et al., 2011).

The most important step, subsequent to the estimation of *H* and LE by remote sensing models, is to validate the results, which is not an easy task due to the lack of accurate and frequent ground observations that is in sync with the spatial resolution of the space-borne remote sensing data (Jia et al., 2003). The recently developed LAS (large aperture scintillometers) can measure *H* averaged over

* Corresponding author. Tel.: +86 10 58993211.
E-mail address: wangyuany@cma.gov.cn (Y. Wang).

0303-2434/$ – see front matter © 2012 Elsevier B.V. All rights reserved.
http://dx.doi.org/10.1016/j.jag.2012.09.005

Table 1
VIRR specifications on-board FY3A.

Band	Bandwidth (μm)	Required noise equivalent reflectivity (temperature) difference
1	0.58–0.68	0.1
2	0.84–0.89	0.1
3	3.55–3.93	0.3*k*
4	10.3–11.3	0.2*k*
5	11.5–12.5	0.2*k*
6	1.55–1.64	0.15
7	0.43–0.48	0.05
8	0.48–0.53	0.05
9	0.53–0.58	0.05
10	1.325–1.395	0.19

horizontal distances comparable to a pixel size of about 1–5 km; thus, it provides a promising solution for the difficulty encountered during validation of the satellite-derived *H* (Hoedjes et al., 2002).

There has been extensive research on the use of LAS measurements for regional flux validation. Jia et al. (2003) evaluated the SEBS model using ATSR data by comparing *H* estimates from three different landscapes to those obtained from the LAS instruments. They found that the total *rmse* (root mean square error) of *H* was approximately 25.5 W/m^2. Irrigation areas with fruit trees showed the highest error. Tang et al. (2011) compared three models (SEBS, TSEB, TVT) using LAS measurements and MODIS data over a wheat-corn production region, and reasonable agreements (*rmse* < 50 W/m^2) were observed between the SEBS and TSEB models. They also found the SEBS model to be more sensitive to errors, in the MODIS LST and LAI products, than the TSEB model. Marx et al. (2008) used the SEBAL method and NOAA images to calculate *H* over the savannah region in West Africa. They found that the satellite-derived *H* was lower than the LAS measurements and that the uncertainties in the instantaneous LE were smaller than the uncertainties in *H*.

In this study, we validated satellite-derived *H* with the LAS instrument and compared two sensors namely, the FY3A-VIRR and TERRA-MODIS. We estimated *H* with the SEBS model over the Alpine grass region in the Qinghai Province of China. This study differs from the earlier studies in two ways. First, it is a relatively long-term validation (May–September 2010) compared to other studies, which used a limited number of images. Therefore, the sample size for validation is larger, and consequently, the seasonal change in *H* estimation accuracy can be also analysed. Second, a new sensor data (viz., FY3A-VIRR, visible and infrared radiometer) is used in the *H* estimations and is compared with its counterpart (TERRA-MODIS), which is novel and informative for researchers interested in VIRR data application. The FY3A, a new generation of polar-orbiting meteorological satellite, was launched on 27 May 2008. VIRR is one of the 11 uploads on the FY3A satellite (Dong et al., 2009). It has 10 bands with a spectral range of 0.44–12.5 μm (see Table 1). The spatial resolution is 1 km, and the local equatorial crossing time is approximately 10:05 am, which is 25 min earlier than the TERRA satellite.

The main objectives of this study are to evaluate the SEBS model performance for our study region and to check if FY3A-VIRR data is qualified for *H* estimation using the MODIS-derived *H* result as a benchmark. In Section 2, a brief description of the SEBS model is provided. In Section 3, the study site, ground data collection methods and remote sensing data processing steps are described. In Section 4, the accuracy of the satellite-derived *H* is validated with the LAS-estimated *H*. Discussion and conclusions are provided in Sections 5 and 6, respectively.

2. The SEBS model

The SEBS model, proposed by Su (2002), is one of the most important and widely used single-source models for estimating *H* and LE (Rwasoka et al., 2011; Jia et al., 2009). Intensive research has been performed to validate the SEBS results for multiple spatio-temporal scales (McCabe and Wood, 2006). Studies also pay attention to the uncertainties and sensitivities of the model inputs (Gilbson et al., 2010; van der Kwast et al., 2009). Su (2002) examined the SEBS model performance in depth with four datasets. He concluded following: (1) Mean error of the SEBS model estimates is expected to be approximately 20% relative to the mean *H*, if the geometric and physical input variables are reliable. (2) Temperature, wind speed, roughness length for heat transfer, and stability corrections have large impacts on the SEBS results. (3) Currently available stability corrections are inadequate for describing the transition period (from stable night condition to unstable daytime condition). Recently, Gokmen et al. (2012) proposed an updated SEBS model that explicitly included the effect of soil moisture availability and obtained satisfactory results for *H* calculation in water-stressed regions. However, the updated model requires spatial information on soil moisture and tuning for several new parameters, making it difficult to apply the model in real world situations. Therefore, in this study, the original SEBS model has been used.

Inputs to the SEBS model include land cover structural parameters (leaf area index, vegetation height, and fractional vegetation cover), meteorological measurements at a reference height (wind speed, humidity, air temperature, and pressure), height of the planetary boundary layer, and remote sensing products such as land surface temperature (LST), albedo (α), emissivity (ε), and NDVI. The SEBS model has three distinctive features compared to other models. First, it has two methods for the estimation of the stability parameters needed for the *H* calculations. If the reference height is below the top of the atmospheric surface layer (ASL), then the Monin–Obukhov similarity functions are invoked, otherwise the bulk atmospheric similarity model is used (Wang et al., 2008). Second, the non-dimensional parameter KB^{-1} is usually adopted as a constant in other models, whereas in the SEBS, the same parameter is calculated on a per pixel basis with an algorithm that combines an earlier full-cover canopy model (Choudhury and Monteith, 1988), a bare land model (Brutsaert, 1999), and a new equation term describing the vegetation-bare soil interaction (Su et al., 2001; Wang et al., 2008; Jia et al., 2003). Third, the radiation balance, *H* and LE under dry and wet limits, and the EFr (Evaporative fraction) are calculated for every pixel (Su, 2002; Gibson et al., 2011).

Given below is a simple description of the method of *H* estimation in the SEBS model. In the ASL, the similarity relationships for the profiles of the mean wind speed *u*, and mean temperature, $\theta_0 - \theta_a$, are usually written in the integral form as

$$u = \frac{u_*}{k}\left[\ln\left(\frac{z-d_0}{z_{0m}}\right) - \Psi_m\left(\frac{z-d_0}{L}\right) + \Psi_m\left(\frac{z_{0m}}{L}\right)\right] \quad (1)$$

$$\theta_0 - \theta_a = \frac{H}{k u_* \rho C_p}\left[\ln\left(\frac{z-d_0}{z_{0h}}\right) - \Psi_h\left(\frac{z-d_0}{L}\right) + \Psi_h\left(\frac{z_{0h}}{L}\right)\right] \quad (2)$$

In the above equations, $k = 0.41$ is the von Karman's constant; z is the reference height (m); u_* is the friction velocity (m/s); ρ is the density of air (kg/m^3); C_p is the specific heat capacity of air (J/kg K); θ_0 and θ_a are the potential air temperatures (K) at the surface and reference height, respectively; z_{0m} is the roughness height for the momentum transfer (m); z_{0h} is the scalar roughness height for the heat transfer (m), $z_{0h} = z_{0m}/\exp(KB^{-1})$; d is the zero-plane displacement height (m); and Ψ_m and Ψ_h are the stability correction functions for momentum and sensible heat transfer, respectively,

which are described in Wang et al. (2008). L is the Obukhov length, defined as

$$L = -\frac{\rho C_p u_*^3 \theta_v}{kgH}, \tag{3}$$

where g is the acceleration due to gravity (m/s^2) and θ_v is the potential virtual temperature near the surface (K).

The three unknown variables in the system of non-linear Eqs. (1)–(3) are u_*, H and L, and they can be solved for by using the Broyden method (Su, 2002).

It is important to indicate that the solution for H described above is independent of the energy balance and only requires the wind speed, air temperature at the reference height, and LST. If the LST or the meteorological variables have large uncertainties, the resultant value of H is affected (Su, 2002). In the SEBS model, this uncertainty is reduced by taking the energy balance of the limiting cases into account – the value of H must fall between the values obtained for H at the two extreme conditions, the wet and dry limits (Su, 2002; Gibson et al., 2011).

In the dry-limit scenario, LE becomes zero, and H_{dry} can be calculated as

$$H_{dry} = R_n - G_0 \tag{4}$$

In the wet-limit scenario, where evaporation takes place at a potential rate, H_{wet} can be calculated as

$$H_{wet} = \frac{R_n - G_0 - (\rho C_p / r_{ew}) \cdot (e_s - e)/\gamma}{1 + (\Delta/\gamma)}, \tag{5}$$

where R_n is net radiation (W/m^2), Δ is the rate of change of the saturation vapour pressure with the temperature (Pa/K), γ is the psychrometric constant (γ = 67 Pa/K), e_s and e are the saturation and actual vapour pressures (Pa) respectively, G_0 is the soil heat flux (W/m^2) calculated as

$$G_0 = R_n \cdot (\Gamma_c + (1 - f_c) \cdot (\Gamma_s - \Gamma_c)) \tag{6}$$

where Γ_c = 0.05 for the full vegetation canopy and Γ_s = 0.315 for the bare soil. An interpolation is performed between these limiting cases using the fractional canopy coverage, f_c (Wang et al., 2008).

3. Data

3.1. Field measurements

The LAS instrument is installed at Arou County, east of the Qinghai province, at an altitude of approximately 3000 m. The site is flat and covered with grasslands, with the grass height being approximately 20–30 cm during the summer. Annual mean air temperature is 1.5 °C. Average annual precipitation is 417 mm. The LAS makes measurements along a path between the transmitter (38°03′24.3″N, 100°28′16.4″E) and receiver (38°02′18.1″N, 100°27′25.9″E), with the distance being 2390 m.

The meteorological observation tower (38°02′39.8″N, 100°27′53.1″E) is installed between the LAS transmitter and receiver. The distance of the tower to the LAS transmitter is 1490 m. The observations include precipitation, pressure, relative humidity, wind speed, temperature at two different heights above the ground (2 m and 10 m), and four component radiations (downwelling, upwelling, shortwave, and longwave radiations). All the measurements, integrated over a 10 min period, are recorded, except for pressure and precipitation, which are averaged over 30 min.

Monin–Obukhov similarity theory is applied iteratively to derive H from the LAS measured signal (the structure parameter of the refractive index, C_n^2) with the aid of the meteorological observations. The LAS-estimated H is line-averaged and integrated over 30 min. For more information on LAS measurement and processing, the reader is directed to Beyrich and De Bruin (2002).

3.2. Remote sensing data

3.2.1. Remote sensing products preparation

Remote sensing products, such as NDVI, LST, albedo, and emissivity, are the key inputs to the SEBS model. For the MODIS sensor, all the products involved can be downloaded from the web http://lpdaac.usgs.gov/. More specifically, the MOD11A1 (daily land surface temperature product with 1 km spatial resolution), MOD13A2 (16-day composited product of Normalised Vegetation Index with 1 km spatial resolution), and MCD43B3 (BRDF/albedo product with 1 km spatial resolution) from May to September 2010, are downloaded and processed.

Remote sensing products for the VIRR sensor, namely, LST, emissivity and NDVI are available and can be downloaded from the web at http://satellite.cma.gov.cn/PortalSite/Ord/Satellite.aspx. The LST product is retrieved with Becker's LST algorithm, and the parameters in the algorithm have been recalculated on the basis of the spectral response function of the VIRR sensor (Yang and Yang, 2006). For more information about VIRR products, please refer to the literature in Yang and Dong (2011).

A key challenge in the estimation of H from the VIRR data is that albedo, a key parameter in R_n calculation, is not an operational product for the VIRR yet. Therefore, the simple method used in the SEBAL model (Waters et al., 2002) was used to produce an approximate estimation of the VIRR albedo and is described below:

$$\alpha_{toa} = \sum (\varpi_\lambda \times \rho_\lambda) \tag{7}$$

$$\varpi_\lambda = \frac{ESUN_\lambda}{\sum ESUN_\lambda} \tag{8}$$

$$\alpha = \frac{\alpha_{toa} - \alpha_{path\_radiance}}{\tau_{sw}^2} \tag{9}$$

$$\tau_{sw} = \frac{R_{s\downarrow}}{R_{s\_TOA}} = \frac{R_{s\downarrow}}{G_0 \times \cos(\text{sun\_zenith}) \times d_r}. \tag{10}$$

In the above equations, α_{toa} is the albedo at the top of the atmosphere (TOA). ρ_λ is the TOA reflectivity for each band. ϖ_λ is the weighing coefficient calculated from the extra atmospheric solar irradiance for each band. $\alpha_{path\_radiance}$ is the average portion of the incoming solar radiation across all bands that is back-scattered before it reaches the earth's surface. We chose a value of 0.03 for $\alpha_{path\_radiance}$ based on the SEBAL recommendation. τ_{sw} is the atmospheric transmissivity and can be calculated by dividing the shortwave radiation TOA by the incoming shortwave radiation measured at surface ($R_{s\downarrow}$). The shortwave radiation TOA can be computed by using the solar constant (G_0 = 1367 W/m^2), the sun zenith angle, and the relative earth–sun distance.

3.2.2. Remote sensing products application

LST, albedo and emissivity are needed in the R_n calculation, which is calculated as follows,

$$R_n = (1 - \alpha)R_{s\downarrow} + \varepsilon \cdot R_{L\downarrow} - R_{L\uparrow} \tag{11}$$

In the above equation, $R_{L\uparrow}$ is the outgoing longwave radiation, and $R_{L\downarrow}$ is the incoming longwave radiation. The two items can be computed using the Stefan–Boltzmann equation with the emissivity and temperature information. ε is the emissivity of the surface. α is the surface albedo. $R_{s\downarrow}$ is the incoming shortwave radiation. As our study region is flat and small, $R_{s\downarrow}$ collected at the meteorological station is taken to be well represented and is used in the R_n calculation for all pixels along the LAS path.

Table 2
Monthly z_{0m} values for the LAS station from May to September 2010.

Time	May	June	July	August	September
z_{0m}	0.0247	0.04187	0.04438	0.05299	0.04048

Empirical equations are used to obtain the LAI, and the fractional vegetation cover (fc) from the NDVI (Wang et al., 2008).

$$\mathrm{LAI} = \sqrt{ndvi \times \frac{1+ndvi}{1-ndvi}} \tag{12}$$

$$fc = \left(\frac{ndvi - ndvi\_\min}{ndvi\_\max - ndvi\_\min}\right)^2 \tag{13}$$

3.3. The geometric parameters

Another important category of input for the SEBS model is the geometric parameter, including the roughness height for the momentum transfer (z_{0m}), the zero-plane displacement height (d_0), and the vegetation height (h). For our study, z_{0m} is calculated using the wind and temperature profile of the meteorological observation tower by the method proposed in Yang et al. (2003). Table 2 shows the results of z_{0m} for all the months. d_0 and h are determined with the empirical equations used in the SEBS model namely,

$$d_0 = z_{0m} \times 4.9 \tag{14}$$

$$h = \frac{z_{0m}}{0.136} \tag{15}$$

3.4. SEBS implementation

From the overpass time of the TERRA and FY3A satellites, we determined the meteorological parameters for the MODIS and VIRR data, respectively. Meteorological observations, namely, wind speed, relative humidity, temperature, and pressure, together with the LST, NDVI, z_{0m}, R_n, emissivity, reference height (10 m), and HPBL (1 km), were then fed into the SEBS model to calculate H.

The remote sensing images with 1 km spatial resolution showed that the LAS transmitter and receiver were on the northeast–southwest diagonal of a 3×3 window (Fig. 1). A more precise technique for comparison is to calculate the weighted average of H based on the LAS footprint (Jia et al., 2003; Su, 2002). After several trials, we found that the technique used had a negligible impact on the actual comparison results. Therefore, we compared the LAS-H at satellite overpass time with the diagonal mean of the SEBS-H.

4. Results analysis

To compare the results of the H estimations, four metrics were chosen, viz., root mean square error ($rmse$), correlation coefficient (r), mean (m), and standard deviation (s). These metrics quantify

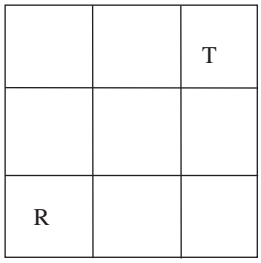

Fig. 1. Location of LAS transmitter (T) and receiver (R) on remote sensing images with 1 km spatial resolution.

Table 3
Comparison results ($rmse$ and r) between VIRR_SEBS_H and VIRR_LAS_H during May–September 2010.

Time	r	$rmse$ (W/m^2)	The number of usable days
May	0.4705	46.9878	13
June	0.1218	65.3973	14
July	0.7817	24.4449	10
August	0.6589	32.8214	16
September	0.4552	40.9485	11
From May to September	0.2159	45.1098	64

Note: The number of usable days indicates that both the LST and LAS-estimated H at satellite overpass time are available.

the performance of the two techniques from different perspectives. For example, $rmse$ is sensitive to the disparities between LAS-H and SEBS-H, r detects how closely SEBS-H follows the LAS-H trend, m checks for over- and under-estimation of H, and s quantifies the fluctuations in the LAS-H and SEBS-H values.

In the following section, we analysed the accuracy of H derived with the SEBS model using both the VIRR data (VIRR_SEBS_H) and the MODIS data (MODIS_SEBS_H). We defined VIRR_LAS_H and MODIS_LAS_H as the LAS-H obtained from the VIRR and MODIS overpass time, respectively.

4.1. Validation of VIRR_SEBS_H using VIRR_LAS_H

Table 3 shows the $rmse$ and r results of the VIRR_SEBS_H and VIRR_LAS_H values. Evidently, July and June show the highest and lowest r (correlation coefficient) respectively. August, May, and September show medium r-values. Very weak positive correlation exists when all the data are aggregated. With respect to $rmse$, July and August show the lowest values, followed by September and May. June shows the highest value. Total $rmse$ is 45.1098 W/m^2, which is 40.57% relative to the mean value of VIRR_LAS_H.

Table 4 shows the statistical comparison between VIRR_SEBS_H and VIRR_LAS_H values. Arguably, VIRR_SEBS_H in May and June is over-estimated and with high fluctuation, whereas from July to September, VIRR_SEBS_H is under-estimated with relatively less fluctuation. Means of VIRR_SEBS_H and VIRR_LAS_H are very close when all the data are aggregated, but standard deviations of VIRR_SEBS_H are still much higher than that of VIRR_LAS_H.

4.2. Validation of MODIS_SEBS_H using MODIS_LAS_H

Table 5 shows the results ($rmse$ and r) of the comparison between the MODIS_SEBS_H and MODIS_LAS_H values. A marked positive correlation is observed for every month except July and May. September has the highest correlation, followed by June and August. Very weak correlation exists when all the data are aggregated. In terms of the $rmse$ metric, the five months can be grouped into two distinct types. May and June show quite high $rmse$ values, whereas the other three months show low $rmse$ values. In particular, $rmse$ in June is the largest, which is in agreement with

Table 4
Comparisons of means and standard deviations of VIRR_SEBS_H and VIRR_LAS_H during May–September 2010.

Time	VIRR_SEBS_H		VIRR_LAS_H	
	m (W/m^2)	s (W/m^2)	m (W/m^2)	s (W/m^2)
May	144.3164	49.5563	126.5682	11.5516
June	140.0309	50.3425	95.8146	8.0178
July	82.9227	29.0954	95.1772	9.7895
August	82.6428	21.2504	111.5327	12.1972
September	89.9441	21.1893	126.7046	11.0751
From May to September	109.0225	45.9303	111.2006	17.0691

Table 5
Comparison results (*rmse* and *r*) between MODIS_SEBS_H and MODIS_LAS_H during May–September 2010.

Time	*r*	*rmse* (W/m^2)	The number of usable days
May	0.3402	72.7142	15
June	0.5034	92.681	14
July	0.0754	20.6987	10
August	0.4271	29.3713	18
September	0.6931	40.8065	14
From May to September	0.1750	58.4654	71

the VIRR_SEBS_H validation. Total *rmse* is 58.4654 W/m^2, which is 50.68% of the mean value of the MODIS_LAS_H.

Table 6 is the statistical comparison between the MODIS_SEBS_H and the MODIS_LAS_H values. Values of MODIS_SEBS_H are clearly over-estimated for May–June and under-estimated for August–September. In July, a moderate over-estimation is also apparent. Standard deviations are large in May and June, and they are less so in the remaining three months. When all the data are aggregated, MODIS_SEBS_H shows persistent over-estimations and intensive fluctuations compared to MODIS_LAS_H.

4.3. Accuracy of VIRR_SEBS_H and MODIS_SEBS_H

Tables 3–6 show the accuracy of VIRR_SEBS_H estimation to be comparable to that of MODIS_SEBS_H estimation. VIRR_SEBS_H shows higher *r* than the MODIS_SEBS_H in May, July, and August, and lower *rmse* than the MODIS_SEBS_H in May, June and July. When all the data from five months are aggregated, VIRR_SEBS_H has slightly better correlation and lower *rmse* values. However, we should not rush to the conclusion that VIRR_SEBS_H has higher accuracy because the number of usable days (sample size available for the validation) is smaller than that of MODIS_SEBS_H and the dates for *H* estimation are not exactly the same.

5. Discussion

5.1. VIRR_SEBS_H performance using MODIS_SEBS_H as a benchmark

5.1.1. Comparison of seasonal change

MODIS_SEBS_H and VIRR_SEBS_H have a similar seasonal change, namely higher in May–June, lower in July–September, and a big reduction from June to July (Fig. 2). However, the seasonal changes differ in the details. The values of MODIS_SEBS_H increase from May to June and decrease from July to September, and June show the highest values. The VIRR_SEBS_H values decrease slightly from May to June, increase from July to September and May show the highest values. Seasonal change of VIRR_SEBS_H is more approximate to LAS_H measurement in that the value of *H* in June is less than in May and the value of *H* in September is higher than in August.

Table 6
Comparisons of means and standard deviations between MODIS_SEBS_H and MODIS_LAS_H during May–September 2010.

Time	MODIS_SEBS_H		MODIS_LAS_H	
	m (W/m^2)	*s* (W/m^2)	*m* (W/m^2)	*s* (W/m^2)
May	168.5445	66.4384	130.1373	9.1367
June	173.7848	66.3449	100.401	20.5603
July	99.0356	19.0293	95.06796	11.3584
August	91.2751	16.4721	115.1934	16.2996
September	92.218	22.1241	129.1914	7.1639
From May to September	125.1481	58.2203	115.3594	19.3515

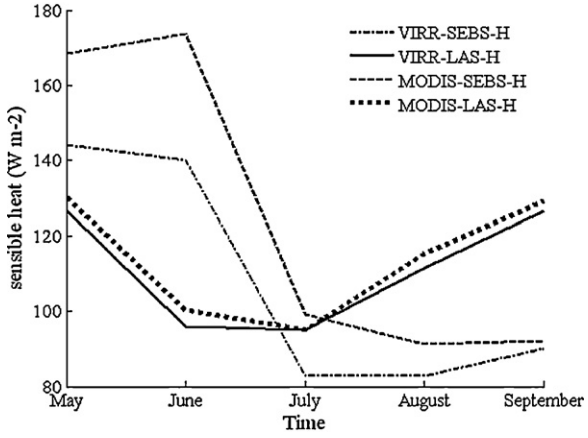

Fig. 2. Temporal variation of sensible heat.

5.1.2. Comparison of monthly averages

As the data used for calculating the MODIS_SEBS_H and VIRR_SEBS_H values were not from the exact same dates, it is more convenient to compare monthly averages. Monthly averages of *H*, LST, air temperature, potential temperature gradient (delta_*T*), EFr, and satellite overpass time are calculated and listed in Table 7.

It is evident from Table 7 that the MODIS/LST is 0.3–2.3 K higher than the VIRR/LST, which is reasonable because the average overpass time of the FY3A satellite is 25 min less than that of the TERRA satellite. delta_*T* of MODIS is 0.7–2.2 K higher than that of VIRR, resulting in a higher value for MODIS_SEBS_H compared to VIRR_SEBS_H because the temperature gradient is the driving force for the sensible heat transfer (Gokmen et al., 2012).

Given the time-dependency of *H*, we compared the EFr (evaporative fraction, i.e., the ratio of LE to the available energy which is often assumed to be constant during the daylight hours) obtained from the VIRR and MODIS data. Results show that the disparity in EFr exists, but to a much less extent than when compared to *H* and LST. The biggest difference occurred in June. For other months, EFr obtained from the MODIS and VIRR data are very similar. It can be expected that VIRR and MODIS data will serve equally well when EFr is used to obtain daily evapotranspiration estimates.

5.1.3. Comparison of spatial patterns

A primary focus of this paper is the LAS validation of SEBS-derived *H* at one location and also to analyse the accuracy changes from May to September. Because there is only one LAS instrument installed around our study site, validation work cannot be conducted on the other parts of the images. However, it is still possible to compare the spatial pattern of *H* derived from the MODIS and VIRR data.

Images acquired on 17 June 2010 were selected because the overpass times of TERRA and FY3A were very close and the cloud cover was low. An image subset (42 km × 31 km in size) covering the LAS instrument and meteorological station was chosen for *H* estimation and subsequent comparison. Fig. 3 shows the result. It is evident that the spatial extent and magnitude of *H* derived from the two sensors are very similar, and *H* is heterogeneous, with values ranging from 50 to 250 W/m^2. The biggest discrepancy is that the MODIS-H result is smoother, whereas VIRR-H result is more granular. As LST is a key parameter in *H* calculation, we also show the image subsets of LST product for the two sensors. Fig. 3 shows that *H* derived from VIRR is influenced because of the granularity of the LST.

Table 7
Monthly means of the main parameters in the SEBS model for MODIS and VIRR from May to September 2010. Abbreviations used are as follows: *H*, sensible heat; LST, land surface temperature; t_pbl, air temperature at the reference height during satellite overpass; delta_*T*, potential temperature gradient; and EFr, evaporative fraction.

	May	June	July	August	September
MODIS					
H (W/m^2)	168.5445	173.7848	99.0356	91.2751	92.218
LST (K)	300.4647	302.7162	298.5733	296.2735	294.5919
t_pbl (K)	283.7050	289.1021	290.6870	288.9800	286.7057
delta_*T* (K)	18.51643	15.02473	8.696569	8.037959	8.6962
EFr	0.6209	0.6688	0.8425	0.8393	0.8055
Overpass time (h) (Beijing time)	12.2666	12.1762	12.1633	12.1889	12.0833
VIRR					
H (W/m^2)	144.3164	140.0309	82.9227	82.6428	89.9441
LST (K)	298.8641	302.1833	296.4100	294.3906	294.2636
t_pbl (K)	283.2370	289.3486	290.5260	288.7975	287.0182
delta_*T* (K)	16.9393	14.1670	6.4889	6.1628	7.9885
EFr	0.6398	0.7399	0.8584	0.8590	0.8076
Overpass time (h) (Beijing time)	11.9295	12.0060	12.1583	11.9323	11.9394

5.2. Sensitivity analysis of H for delta_T

Table 7 shows that *H* displays the same seasonal change as delta_*T*, a finding that has been previously reported by Bodola (2009) and Gibson et al. (2011). During May–June, delta_*T* and *H* are large, whereas during July–September, delta_*T* and *H* are comparatively lower. The correlation coefficient between delta_*T* and *H* is 0.7551 for VIRR and 0.7703 for MODIS when all the data are aggregated. However, the correlation coefficients vary from month to month. *H* is constrained to be within the possible extrema calculated for the wet and dry limit. Therefore, when an extreme condition is reached, the relationship between delta_*T* and *H* would change (Bodola, 2009; Gibson et al., 2011).

To explore the influences of delta_*T* on *H* under different conditions, we took z_{0m} and wind speed, key parameters in the SEBS model, into account. MODIS remote sensing data on 1st September, and the corresponding meteorological measurements are selected randomly to provide initial values for the model inputs (see Table 8).

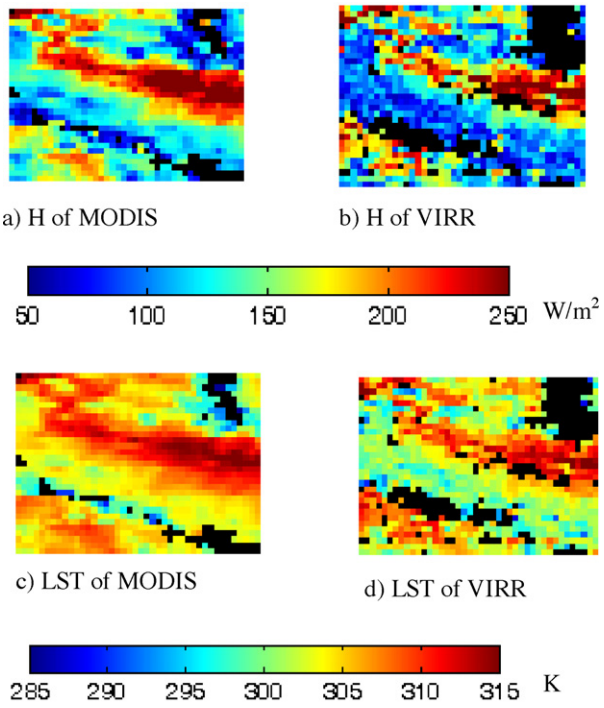

Fig. 3. Comparison of the spatial pattern of *H* and LST between MODIS and VIRR. The image subset is 42 km × 31 km in size and covers the LAS instrument and meteorological station. MODIS image is acquired at 04:26 (UTC), 17 June 2010, and VIRR image is acquired at 04:15 (UTC), 17 June 2010. Black indicates cloud cover.

First, we performed a sensitivity analysis by the variation of delta_*T* and z_{0m} while wind speed was kept unchanged. LST increased by 20 K with a step size of 1 K and z_{0m} increased (decreased) by 0.03 with a step of 0.01 (−0.01). Results are shown in Fig. 4(a), which points to some interesting phenomena as well: (1) *H* is not always positively correlated with delta_*T*. There exists an inflection point, which is caused by replacing *H*, derived from the non-linear Eqs. (1)–(3), by H_{wet} calculated using Eq. (5). On the left of the inflection point, *H* (H_{wet}) is negatively correlated, whereas on the right, it is positively correlated with delta_*T* and z_{0m}. (2) The *H* values at the inflection points are the lowest and the location of the inflection points are related to the values of z_{0m}. Higher z_{0m} values push the inflection point more towards the left, with little effect on *H*, which indicates that the value is dependent on other model inputs as well. (3) *H* is more sensitive to z_{0m} under high delta_*T* values. When delta_*T* is small, variations in z_{0m} have lesser impact on *H*.

Second, we changed delta_*T* and wind speed values while the value of z_{0m} was kept unchanged. LST was increased by 20 K at steps of 1 K and wind speed was increased to 9.388 m/s from its initial values (1.388 m/s) at steps of 1 m/s. Results are shown in Fig. 4(b). It is evident that *H* and wind speed are closely related. The higher the wind speed, the higher the *H* value. In scenarios with high delta_*T* values, an increase in wind speed causes a large increase in *H*. By contrast, when delta_*T* is small, wind speed has little effect on *H*. Inflection points like those that appear in Fig. 4(a) only exist when the wind speed is low. Because *H* cannot exceed H_{dry}, a flat line appears on the top right of Fig. 4(b), which implies that *H* would not change after the dry limit is reached.

From the sensitivity analysis above, we can conclude that (1) delta_*T* and *H* are positively correlated except at extreme conditions and (2) the variation in *H* calculation is very large when delta_*T* is high, which explains why *H* estimation during May–June is accompanied with large fluctuations. When delta_*T* is small, it has a more

Table 8
Parameter values used in the sensitivity analysis.

Inputs	Initial values	Change range
LST	292.26 K	Δ = 1, 2, . . ., 20 K
z_{0m}	0.04187	Δ = −0.03, −0.02, . . ., 0.02, 0.03
Wind speed	1.388 m/s	Δ = 1, 2, 3, . . ., 7
Relative humidity	39.71%	Unchanged
Net radiation	751.426 W/m^2	Unchanged
Pressure	71,340 Pa	Unchanged
NDVI	0.6581	Unchanged
Air temperature	284.34 K	Unchanged

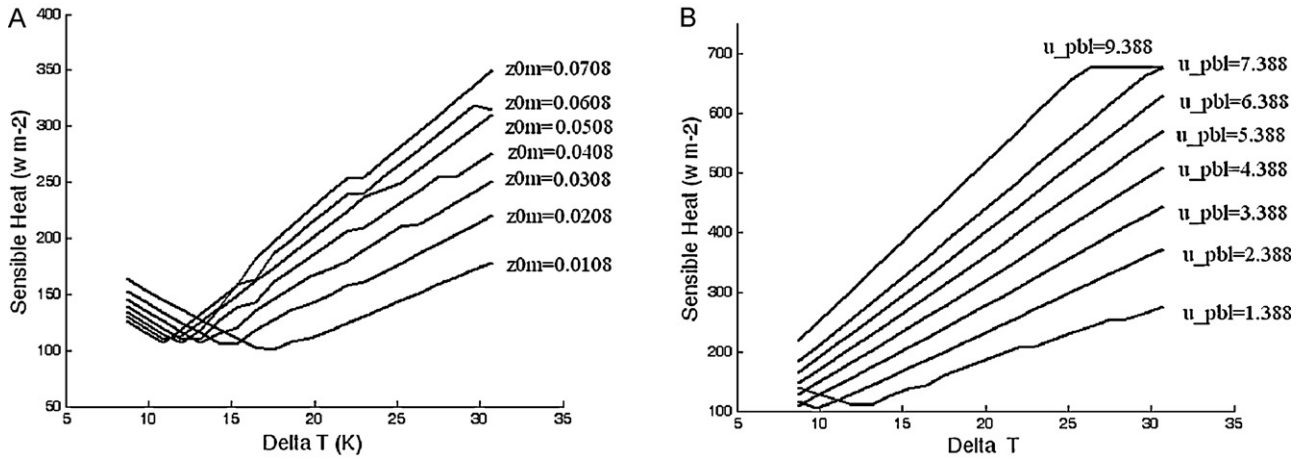

Fig. 4. Sensitivity analysis of H for delta_T. Values of z_{0m} and wind speed (u_pbl) data are extracted from September 1st at MODIS overpass time. The initial values of all the model inputs are listed in Table 8. (a) LST is increased by 20k in steps of 1k and z_{0m} is increased and decreased by 0.03 in steps of 0.01. Other inputs remain unchanged. (b) LST is increased by 20k in steps of 1k and wind speed is increased by 8 m/s in steps of 1 m/s. Other inputs remain unchanged.

dominant role in the determination of H; therefore, H estimation during July–September is accompanied with small fluctuations.

5.3. Analysis of H estimation in June

As a single source model, the SEBS model performs better over densely vegetated area, so SEBS-H, including VIRR_SEBS_H and MODIS_SEBS_H, shows lower *rmse* values during July–September and higher *rmse* values during May–June. The most unexpected result is that SEBS-H in June is the worst. It is more instructive to observe the trends shown in Fig. 2; LAS-H shows an abrupt reduction from May to June, while SEBS-H is still at a high level in June. To further constrain the change in H from May to June, we investigated NCEP reanalysis data downloaded from http://dss.ucar.edu/datasets/ds083.2/. These data are provided every 6 h with a spatial resolution of $1^\circ \times 1^\circ$. First, we determined the grid in which our study site is located. Next, we obtained the H of this grid for the TERRA satellite overpass time with linear interpolation. It is found out that the mean value of H is 196.4626 W/m^2 in May and 121.2787 W/m^2 in June, confirming that H decreases significantly from May to June. We checked the inputs fed into SEBS and found that delta_T and wind speed could be the reason for the over-estimation in June. delta_T is high and windy days are frequent in June, the combined effect of which is a dramatically higher H estimation. Another reason is probably because June is a transitional period from bare land to dense vegetation cover, and thermal dynamic state of the land surface is complicated, which decreases the potential of the SEBS model. In the future, a two-source model will be used to check if better results can be obtained for the month of June.

6. Conclusions

This paper presents a comparison of the FY3A/VIRR and the TERRA/MODIS with respect to H calculation with a single-source model (SEBS) in an alpine grass landscape. A LAS instrument is used to validate the satellite-derived H values. Following are the conclusions from this study:

(1) H estimation accuracy of VIRR is similar to that of MODIS, which indicates that VIRR data quality is as good as that of MODIS under normal conditions. EFr, which can be assumed to be time-independent, shows good agreement between MODIS and VIRR.
(2) During July–September, H estimation (including retrieved from MODIS and VIRR data) has lower *rmse* values, fewer fluctuations and slight underestimations. However, in May–June, H estimation has larger *rmse* values, bigger fluctuations and ample overestimations.
(3) The SEBS model over-estimates H in June, probably because of high wind speed, large delta_T, and complicated thermodynamic state. More in-depth research is needed to address this phenomenon.

Acknowledgement

The work is supported by the R&D Special Fund for Public Welfare Industry (Meteorology), Project Nos. GYHY(QX)2007-6-46 and GYHY200906041-02

References

Allen, R.G., Tasumi, M., Trezza, R., 2007. Satellite-based energy balance for mapping evapotranspiration with internalized calibration (METRIC)-model. Journal of Irrigation and Drainage Engineering 133, 380–394.
Bastiaanssen, W.G.M., 2000. SEBAL based sensible and latent heat fluxes in the irrigated Gediz Basin, Turkey. Journal of Hydrology 229, 87–100.
Beyrich, F.R., De Bruin, H.A., 2002. Results from one-year continuous operation of a large aperture scintillometer over a heterogeneous land surface. Boundary Layer Meteorology 105, 85–97.
Bodola, A., 2009. Validation of surface energy balance system (SEBS) over forest land cover and sensitivity analysis of the model. MSc Thesis. International Institute for Geo-information Science and Earth Observation, The Netherlands.
Brutsaert, W., 1999. Aspects of bulk atmospheric boundary layer similarity under free-convective conditions. Reviews of Geophysics 37, 439–451.
Choudhury, B.J., Monteith, J.L., 1988. A four-layer model for the heat budget of homogeneous land surfaces. Quarterly Journal of the Royal Meteorological Society 114, 373–398.
Courault, D., Seguin, B., Olioso, A., 2005. Review on estimation of evapotranspiration from remote sensing data: from empirical to numerical modeling approaches. Irrigation and Drainage System 19, 223–249.
Dong, C.H., Yang, J., Zhang, W.J., Yang, Z.D., Lu, N.M., Shi, J.M., Zhang, P., Liu, Y.J., Cai, B., 2009. An overview of a new Chinese weather satellite FY-3A. Bulletin of the American Meteorological Society 90, 1531–1544.
Gilbson, L.A., Munch, Z., Engelbrecht, J. Petersen, N., and Conrad, J.E., 2010. Remote sensing as a tool for resources assessment towards the determination of the legal compliance of surface and groundwater use, Water Research Commission, Pretoria, South Africa, WRC Report No. 1690/1/09.
Gibson, L.A., Münch, Z., Engelbrecht, J., 2011. Particular uncertainties encountered in using a pre-packaged SEBS model to derive evapotranspiration in a heterogeneous study area in South Africa. Hydrology and Earth System Sciences 15, 295–310.
Gokmen, M., Vekerdy, Z., Verhoef, A., Verhoef, W., Batelaan, O., van der Tol, C., 2012. Integration of soil moisture in SEBS for improving evapotranspiration estimation under water stress conditions. Remote Sensing of Environment 121, 261–274.

Hoedjes, J.C.B., Zuurbier, R.M., Watts, C.J., 2002. Large aperture scintillometer used over a homogeneous irrigated area partly affected by regional advection. Boundary Layer Meteorology 105, 99–117.

Jia, L., Su, Z., van den Hurk, B., Menenti, M., Moene, A., De Bruin, H., Javier Baselga Yrisarry, A.R., Ibanez, J., Cuesta, M.A., 2003. Estimation of sensible heat flux using the surface energy balance system (SEBS) and ATSR measurements. Physics and Chemistry of the Earth 28, 75–88.

Jia, L., Xi, G., Liu, S., Huang, C., Yan, Y., Liu, G., 2009. Regional estimation of daily to annual regional evapotranspiration with MODIS data in the Yellow River Delta wetland. Hydrology and Earth System Sciences 13, 1775–1787.

Li, Z.L., Tang, R.L., Wan, Z.M., Bi, Y.Y., Zhou, C.D., Tang, B.H., Yan, G.J., Zhang, X.Y., 2009. A review of current methodologies for regional evapotranspiration estimation from remotely sensed data. Sensors 9, 3801–3853.

Marx, A., Kunstmann, H., Schüttemeyer, D., Moene, A.F., 2008. Uncertainty analysis for satellite derived sensible heat fluxes and scintillometer measurements over Savannah environment and comparison to mesoscale meteorological simulation results. Agricultural and Forest Meteorology 148, 656–667.

McCabe, M.F., Wood, E.F., 2006. Scale influences on the remote estimation of evapotranspiration using multiple satellite sensors. Remote Sensing of Environment 105, 271–285.

Moran, M.S., Clarke, T.R., Inoue, Y., Vidal, A., 1994. Estimating crop water deficit using the relationship between surface-air temperature and spectral vegetation index. Remote Sensing of Environment 49, 246–363.

Norman, J.M., Kustas, W.P., Humes, K.S., 1995. A two-source approach for estimating soil and vegetation energy fluxes in observations of directional radiometric surface temperature. Agricultural and Forest Meteorology 77, 263–293.

Roerink, G.J., Su, Z., Menenti, M., 2000. S-SEBI: a simple remote sensing algorithm to estimate the surface energy balance. Physics and Chemistry of the Earth (B) 25 (2), 147–157.

Rwasoka, D.T., Gumingdoga, W., Gwenzi, J., 2011. Estimation of actual evapo transpiration using the surface energy balance system (SEBS) algorithm in the Upper Manyme catchment in Zimbabwe. Physics and Chemistry of the Earth 36, 739–746.

Tang, R., Li, Z., Jia, Y., Li, C., Sun, X., Kustas, W.P., Anderson, M.C., 2011. An intercomparsion of three remote sensing-based energy balance models using large aperture scintillometer measurements over a wheat-corn production region. Remote Sensing of Environment 115, 3187–3202.

Timmermans, W.J., van der Kwast, J., Gieske, A.S.M., Su, Z., Olioso, A., Jia, Li., Elbers, J., 2005. Intercomparison of energy flux models using ASTER imagery at the SPARC 2004 site, Barrax, Spain. In: Proceedings of the ESA WPP-250: SPARC Final Workshop, Enschede, 4–5 July.

Vinukollu, R.K., Wood, E.F., Ferguson, C.R., Fisher, J.B., 2011. Global estimates of evapotranspiration for climate studies using multi-sensor remote sensing data: evaluation of three process-based approaches. Remote Sensing of Environment 115, 801–823.

van der Kwast, J., Timmermans, W., Gieske, A., Su, Z., Jia, L., Elbers, J., Karssenberg, D., de Jong, S., 2009. Evaluation of the surface energy balance system (SEBS) applied to ASTER imagery with flux-measurements at the SPARC 2004 site (Barrax, Spain). Hydrology and Earth System Sciences 13, 1337–1347.

Wang, L., Parodi, G.N., Su, Z., 2008. SEBS MODULE SEAM: a practical tool for surface energy balance estimates from remote sensing data. In: Lacoste, H., Ouwehand, L. (Eds.), Proc. of the '2nd MERIS/(A) ATSR User Workshop'. Frascati, Italy, p. 7.

Waters, R., Allen, R., Bastiaanssen, W., Tasumi, M., Trezza, R., 2002. SEBAL, Surface Energy Balance Algorithms for Land, Advanced Training and Users Manual, Version, 1.0, pp. 16–24.

Yang, K., Koike, T., Yang, D.W., 2003. Surface flux parameterization in the Tibetan plateau. Boundary Layer Meteorology 116, 245–262.

Yang, J., Dong, C.H., 2011. Operational Products and Application for the New Generation of Polar-orbiting FY Meteorological Satellites. Science Press, Beijing, pp. 214–218 (in Chinese).

Yang, H., Yang, Z.D., 2006. A modified land surface temperature split window retrieval algorithm and its applications over China. Global and Planetary Change 52, 207–215.

Su, Z., Schmugge, T., Kusta, W.P., et al., 2001. An evaluation of two models for estimation of the roughness height for heat transfer between the land surface and the atmosphere. Journal of Applied Meteorology 40, 1933–1951.

Su, Z., 2002. The surface energy balance system (SEBS) for estimation of turbulent heat fluxes. Hydrology and Earth System Sciences 6 (1), 85–99.